UNIVERSITY OF BATH

Citation for published version:
Plugaru, N, Nemnes, GA, Filip, L, Pintilie, I, Pintilie, L, Butler, KT & Manolescu, A 2017, 'Atomistic Simulations of Methylammonium Lead Halide Layers on PbTiO3 (001) Surfaces', Journal of Physical Chemistry C, vol. 121, no. 17, pp. 9096-9109. https://doi.org/10.1021/acs.jpcc.7b00399

DOI:
10.1021/acs.jpcc.7b00399

Publication date:
2017

Document Version
Peer reviewed version

Link to publication

This document is the Accepted Manuscript version of a Published Work that appeared in final form in Journal of Physical Chemistry C, copyright © American Chemical Society after peer review and technical editing by the publisher. To access the final edited and published work see https://doi.org/10.1021/acs.jpcc.7b00399.

University of Bath

General rights
Copyright and moral rights for the publications made accessible in the public portal are retained by the authors and/or other copyright owners and it is a condition of accessing publications that users recognise and abide by the legal requirements associated with these rights.

Take down policy
If you believe that this document breaches copyright please contact us providing details, and we will remove access to the work immediately and investigate your claim.

Download date: 13. May. 2019

Atomistic Simulations of Methylammonium Lead Halide Layers on $PbTiO_3$ (001) Surfaces

Neculai Plugaru,[*,†] George Alexandru Nemnes,[‡,¶] Lucian Filip,[†] Ioana Pintilie,[†] Lucian Pintilie,[†] Keith Tobias Butler,[§] and Andrei Manolescu[‖]

National Institute of Materials Physics, Magurele, 077125 Ilfov, Romania, University of Bucharest, Faculty of Physics, Materials and Devices for Electronics and Optoelectronics ResearchCenter, Magurele, 077125 Ilfov, Romania, Horia Hulubei National Institute for Physics and Nuclear Engineering, Magurele, 077126 Ilfov, Romania., Centre for Sustainable Chemical Technologies and Department of Chemistry, University of Bath, Claverton Down, Bath BA2 7AY, UK, and School of Science and Engineering, Reykjavik University, Menntavegur 1, IS-101 Reykjavik, Iceland.

E-mail: plug@infim.ro

Phone: +40 212 418 221. Fax: +40 213 690 177

[*]To whom correspondence should be addressed

[†]National Institute of Materials Physics, Magurele, 077125 Ilfov, Romania

[‡]University of Bucharest, Faculty of Physics, Materials and Devices for Electronics and Optoelectronics ResearchCenter, Magurele, 077125 Ilfov, Romania

[¶]Horia Hulubei National Institute for Physics and Nuclear Engineering, Magurele, 077126 Ilfov, Romania.

[§]Centre for Sustainable Chemical Technologies and Department of Chemistry, University of Bath, Claverton Down, Bath BA2 7AY, UK

[‖]School of Science and Engineering, Reykjavik University, Menntavegur 1, IS-101 Reykjavik, Iceland.

Abstract

The substantial increase in the power conversion efficiency of hybrid perovskite solar cells, to date reaching more than 20% in laboratory, has strongly motivated research on this class of organic-inorganic materials and related devices, particularly based on $CH_3NH_3PbI_{3-x}X_x/TiO_2$ heterostructures (X=Cl,Br). Taking under consideration that a ferroelectric substrate may act as an efficient electron transporter, positively influencing charge collection across the interface and allowing the tuning of the halide perovskite (HP) - ferroelectric junction, we performed extensive density functional theory calculations on $CH_3NH_3PbI_{3-x}Cl_x$ layers deposited on tetragonal $PbTiO_3$ (PTO) (001) surfaces, to study their structural and electronic properties. The main findings of this study are: *i)* A ferroelectric polarization pointing from the PTO/HP interface to the PTO is favourable for the photogenerated electrons transfer across the interface and their transport to the collecting electrode; *ii)* The PTO internal electric field leads to a position dependent energy levels diagram; *iii)* The HP gap may be tuned by chlorine concentration at the interface, as well as the by the surface terminations of $PbTiO_3$ and hybrid perovskite layers; *iv)* The presence of the PTO ferroelectric surface is likely to have just a slight orientational effect on the $(CH_3NH_3)^+$ dipoles.

1 Introduction

Recently, the hybrid halide perovskites (HPs), particularly $CH_3NH_3MX_3$, where M= Pb or Sn and X= Cl, Br or I, have stirred up a huge research interest, showing both an unprecedented progress in the attainable power conversion efficiency (PCE) of solar cells, as well as an attractive potential for use in a variety of other optoelectronic applications, including LEDs, lasers and sensors.[1–6] Thorough studies performed by ab-initio molecular dynamics and Monte Carlo simulations have predicted that the whirling motion of the organic molecule and associated electrical dipole would exert an influence on carriers distribution, ionic transport, and ferroelectric domain structure, with consequences such as frequency-dependent

permittivity, low electron-hole recombination rates, and current-voltage hysteresis in hybrid halide photovoltaic cells.[7–10] Although it is becoming clear that at room temperature most HPs are not fully ferroelectric, the formation of local regions of polarized domains, in a relaxor ferroelectric scenario, is much more likely. It has also been rationalized that the hybrid perovskites may exhibit a significant enhancement of photoferroic processes at the nanoscale.[8,11] Studies of carrier recombination and mobility mechanisms, responsible for the outstanding diffusion lengths in the HPs,[12] the exciton binding energy and effective masses,[13] as well as the nature of carrier scattering mechanisms and electron-phonon coupling,[14] have brought more insight into the fundamental properties of this class of materials, providing clues on further practical improvements.

Previous investigations on the crystal structure of $CH_3NH_3PbX_3$, ($MAPbX_3$), found that these materials are soft as regards the temperature dependence of their structural and physical properties.[15–17] The perovskite cubic structure, with space group (S.G.) symmetry Pm-3m, is preferred at high temperature, and a tetragonal phase, S.G. I4/mcm, establishes at intermediate temperature range, whereas an orthorhombic phase, S.G. Pnma, is adopted down to the lowest temperature. In the cubic phase, the large methylammonium (MA) molecule, $(CH_3NH_3)^+$, resides at the 1b site (cuboctahedral) as the A cation in the cubic ABO_3 perovskites, and the divalent Pb cation occupies the 1a site (octahedral), with bonding to the halide ion, X, forming a $(PbX_3)^-$ complex. A recent detailed structural analysis of x-ray diffraction data of $MAPbI_3$ confirmed the structural phase transformations, and assessed by transmission electron microscopy a 'pseudo-cubic' structure behaviour consistent with variability in the PbX6 octahedra tilting.[18] These results are well supported by first-principles density functional theory (DFT) calculations, which underline that at the origin of the octahedral tilting in halide perovskites is the hydrogen bonding between the organic cation and the halide frame.[19] Although the calculations were performed on the (ordered) orthorhombic structure of $MAPbI_3$, the authors emphasize that their findings are also relevant to (disordered) tetragonal and cubic $MAPbI_3$ phases, in which the tilts dynamics manifests

as soft phonon modes.

A rather intriguing perspective has been revealed since enhanced carrier mobilities and significantly reduced recombination rates were found in mixed halides $CH_3NH_3PbX_{3-x}Z_x$, (X, Z= I, Cl, Br) compared to pure HPs.[20–24] In the search of the microscopic mechanisms that could explain these effects it was inferred from XPS data,[25] that only small amounts of chlorine substitute for iodine in the perovskite layer, while the chlorine in excess concentrates near the interface. However, the synthesis of $CH_3NH_3PbI_2Cl$ in the tetragonal phase has also been reported as possible.[26] On the theoretical side, a study by first principles methods of the morphology and electronic structure of $MAPbI_{3-x}Cl_x$ on anatase TiO_2 surfaces has concluded that interfacial chlorine may determine the preferential growth of (110) surfaces on TiO_2, due to an increased binding energy of $MAPbI_{3x}Cl_x$ compared to $MAPbI_3$, and thus favor higher electron injection.[27] Also, electronic structure calculations carried on $MAPbI_{3-x}Cl_x$/rutile-TiO_2 layers have shown that interfacial Cl determines an oscillating charge density on the TiO_2 side of the junction, which may favourably contribute to electron transport across the interface.[28]

One has also to consider that the realisation of a photovoltaic device involves, besides the light absorber material, also the presence of layers for carriers extraction and their transport to the collecting electrodes. The composition, morphology and intrinsic properties of these layers, as well as the characteristics of the interfaces they form with the absorber layer play a critical role in the overall energetic performance of the heterostructure.[29] From this perspective, an interesting approach is to consider a heterostructure between the HP layer and a polarized surface, aiming to understand the effects of polarization on the local structure details, bonding and electronic states at the interface, as well as carriers transport. Indeed, several investigations have shown that the polarization of a substrate influences the structure and interactions at its surface. For example, it was reported that: *i)* the built-in electric fields due to polarization-induced charges in AlGaN/GaN field effect transistors allow very high electron densities to be obtained without any spillover effects.[30] It was proven theoreti-

cally that donor-like surface states are a likely source of the 2D electron gas in AlGaN/GaN heterojunctions, and experimentally confirmed in the case of undoped $Al_0.34Ga_0.66N$/GaN. Also, subtle phenomena, such as structure reconstruction and defective state related to polarization orientation and polarization charge were evidenced at $BiFeO_3/La_xSr_{1-x}MnO_3$ interfaces;[31] *ii)* both the structural details and the electrical polarization at the surface of a ferroelectric influence the molecular adsorption processes (see, e.g.,[32–35] and references cited therein); *iii)* the experimental observations of charge density modulation in graphene deposited on $LiNbO_3$, phenomenologically interpreted as compensation of the ferroelectric polarization by n- or p-doping for ferroelectric polarization pointing towards or away from graphene, respectively, was explained in a model which assumes that the coupling is highly dependent on the net surface-bound charge of the ferroelectric;[36] *iv)* a self-doping process taking place in epitaxial ferroelectric $Pb(Zr_0.2Ti_0.8)O_3$ films, and consisting in the generation of oxygen and cation vacancies which act as donors/acceptors, may account for the compensation of the depolarization field within the film.[37] A matter of utmost importance for the applications of the ferroelectric (FE) thin/ultrathin films and nanostructures is that of the polarization stability and the critical thickness/size.[38–44] Theoretically, it has been shown that a thickness down to 3 unit cells, i.e. about 1.2 nm, is enough to enable the existence of ferroelectricity at room temperature,[45] which is in qualitative agreement with the Berry's phase calculations of polarization and synchrotron radiation x-ray diffraction results reported for PTO,[46–48] supporting a linear decay of the polarization for film thicknesses of about 12 nm down to 4 unit cells.

Following the idea that a built-in electric field in a photovoltaic device may be advantageous for the mechanism of charge separation and charge transfer throughout the structure, we conducted a study using first-principles methods on systems consisting of $CH_3NH_3PbI_{3-x}Cl_x$ layers deposited on the FE $PbTiO_3$ (001) surface. The main results are relevant to the effect of the PTO polarization, as well as the PTO and HP layer terminations on the fundamental electronic properties of the model structures, including band alignment,

charge density distribution and Hartree potential, with emphasis on the HP-PTO interface. The article is organized as follows. In Section 2 we present the computational details and the main features of the structural models used in this work. The results and their discussion with reference to already published reports are exposed in Section 3. The main conclusions of our study are summarized in the final Section of this contribution, also aiming to draw guidelines for the realization of high PCE solar cells based on halide perovskite-ferroelectric oxide perovskite structures.

2 Computational details and model structures

2.1 Method

The DFT calculations in this work were carried out using the Quantum ESPRESSO 5.2.1 code.[49] The geometry optimization and atomic relaxations were performed using the Broyden-Fletcher-Goldfarb-Shanno (BFGS) algorithm,[50] within the generalized gradient approximation (GGA), and the exchange and correlation potential in the PBESol parametrization.[51,52] We employed scalar-relativistic Vanderbilt ultrasoft pseudopotentials,[53] from the QE library.[54] Their transferability was confirmed in the calculations of the equilibrium structures of the bulk constituents from which the model systems were further built. All self-consistent calculations were performed using a kinetic-energy cut-off for the plane waves of 70 Ry. The Brillouin zone integration was performed on an automatically generated Monkhorst-Pack,[55] $4 \times 4 \times 4$ k-mesh in the preoptimization step of bulk systems, and $4 \times 4 \times 1$ k-mesh in the case of the calculations on slabs. A Marzari-Vanderbilt electron energy level smearing with width of 0.07 eV was used for the systems showing a metallic character. The total energy per atom was converged to less than 10^{-3} eV for all calculations, and a dipole correction was applied in order to remove the electrostatic interaction between the surface charges along the z-axis of broken symmetry.[56,57] While the GGA-PBESol approach produces band gap values for $MAPbI_3$ and $MAPbCl_3$ in fair agreement with the experimental

ones, it considerably underestimates the band gap of the $PbTiO_3$, see Table 1 (also, Figure S1 in Supporting Information). Then, as a prerequisite for further reliable results on slabs, we used the DFT+U,[58–60] full implementation in QE, in which both the on-site Coulomb interaction and the on-site exchange interaction are accounted for by the Hubbard U and Stoner J terms, respectively, applied to the Ti 3d and O 2p orbitals.[61–63] The importance of taking into account the on-site Coulomb interaction not only on the TM but also on oxygen has been previously emphasized.[64,65] Several test calculations were performed with U taking values between 4 and 10 eV for Ti 3d and O 2p orbitals, and J between 0.6 and 1.0 eV for Ti 3d. Finally, the values U= 8 eV and J= 0.7 eV for Ti 3d orbitals and U= 8 eV and J= 1.d-4 eV for O 2p, in the atomic projection scheme were used, yielding a band gap of 2.94 eV (see Figures S2a,b in Supporting Information), in fair agreement with experiment, as well as with the details of previously calculated band structure.[66]

Recently, it has been emphasized the importance of including the spin-orbit coupling effect on both the kinetic energy and electron self-energy,[67] in order to correctly describe the band gaps and the spectral properties of the hybrid perovskites, which contain heavy elements such as Pb and I. Following this idea, we performed fully relativistic calculations using the PBE0 hybrid functional, with 25% exact (Hartree-Fock) exchange,[68–71] and optimized norm conserving Vanderbilt pseudopotentials from the Schlipf-Gygi library.[72,73] However, while the results for the $MAPbX_3$ are in fair agreement with the experimental and theoretical ones, see Table 1, this line of approach could not be applied to slabs (containing between 100 and 200 atoms) as the calculations proved to be exceedingly time-consuming. It has previously been shown that GGA underestimates the gap by around 1.3 eV compared to GW, but that SOC reduces the GW gap by around 1.1 eV, therefore the GW+SOC gap is very similar to that obtained with straight GGA and no SOC.[67] This fortuitous cancellation of errors means the band energies of HPs from GGA are very close to the more accurate values including exchange effects and SOC, and consequently, for our interface models it is possible to obtain detailed information about band edge positions with a GGA representation of the HP layer

and GGA+U representation of the PTO layer.

Table 1: Lattice constants, a_0 , b_0 and c_0, unit cell volume, V_0, and band gap, E_g, of structurally optimized $PbTiO_3$ and $MAPbI_{3-x}Cl_x$, with x= 0, 1, 2 and 3.

	$PbTiO_3$ [a]	$MAPbI_3$ [b]	$MAPbI_2Cl$	$MAPbICl_2$	$MAPbCl_3$ [b]
a_0 [Å]	3.8735 (-0.81 %)	6.3125 (-0.36%)	5.6055	5.7600	5.6351 (-0.79%)
b_0 [Å]		6.2201 (-0.86%)	6.2786	5.6065	5.5993 (-1.42%)
c_0 [Å]	4.2034 (1.14 %)	6.3908 (1.49%)	6.3993	6.3173	5.7935 (2.00%)
V_0 [Å^3]	63.07 (-0.50 %)	250.88 (0.96%)	224.12	203.99	182.78 (-0.26%)
E_g [eV] GGA, PBESol	1.68	1.60	1.69	1.99	2.36
E_g [eV] PBE0, SOC		1.80	1.85	2.07	2.41
E_g [eV] exp.	3.45-3.6 [c]	1.61 [d]			3.11 [e]

[a] Between parentheses, relative variations with reference to Glazer and Mabud,[74]
[b] Between parentheses, relative variations with reference to Walsh et al.[75]
[c] Brehm et al.[76]
[d] Yamada et al.[77]
[e] Kitazawa et al.[78]

2.2 Model structures

The model structures were assembled from structurally pre-optimized tetragonal $PbTiO_3$ and $MAPbI_{3-x}Cl_x$ unit cells, with the lattice constants and unit cell volumes listed in Table 1. As a starting point we chose to use the 'pseudo-cubic' structures of the hybrid perovskites, (Figure S3a in Supporting Information), and performed the structure optimization using space group P1. Actually, the cubic symmetry is close to the structure which is present in the experimental device at the operation temperature, the highest temperature of the transition from tetragonal to cubic phase being 327.4 K for the $MAPbI_3$.[15] In the pre-optimization stage, we used as input data for PTO the parameters at 298 K taken from Ref.[74] and for the 'pseudo-cubic' $MAPbI_3$ and $MAPbCl_3$, the data reported by Walsh et al..[75] The equilibrium structural parameters of the hypothetic $MAPbI_2Cl$ and $MAPbICl_2$ were determined starting from several scenarios, in which Cl replaces I in $MAPbI_3$ and I replaces Cl in $MAPbCl_3$, with different random I/Cl distributions. It is worth noting that the total energy (per formula unit)) and the unit cell volumes of the various structurally optimized scenarios (four for each stoichiometry) spanned narrow ranges, of 15 meV and 1.8% respectively for $MAPbI_2Cl$, and 152 meV and 3.7% respectively for the $MAPbICl_2$. At the same time, the mixed halides

show a distortion from the 'pseudo-cubic' to a 'pseudo-tetragonal' structure, which may be assigned to the neglect of the MA molecule dynamics. Consequently, we suggest that the actual in-plane lattice constant (i.e. considering the MA dynamics) should have values in-between those given for a_0 and b_0 in Table 1.

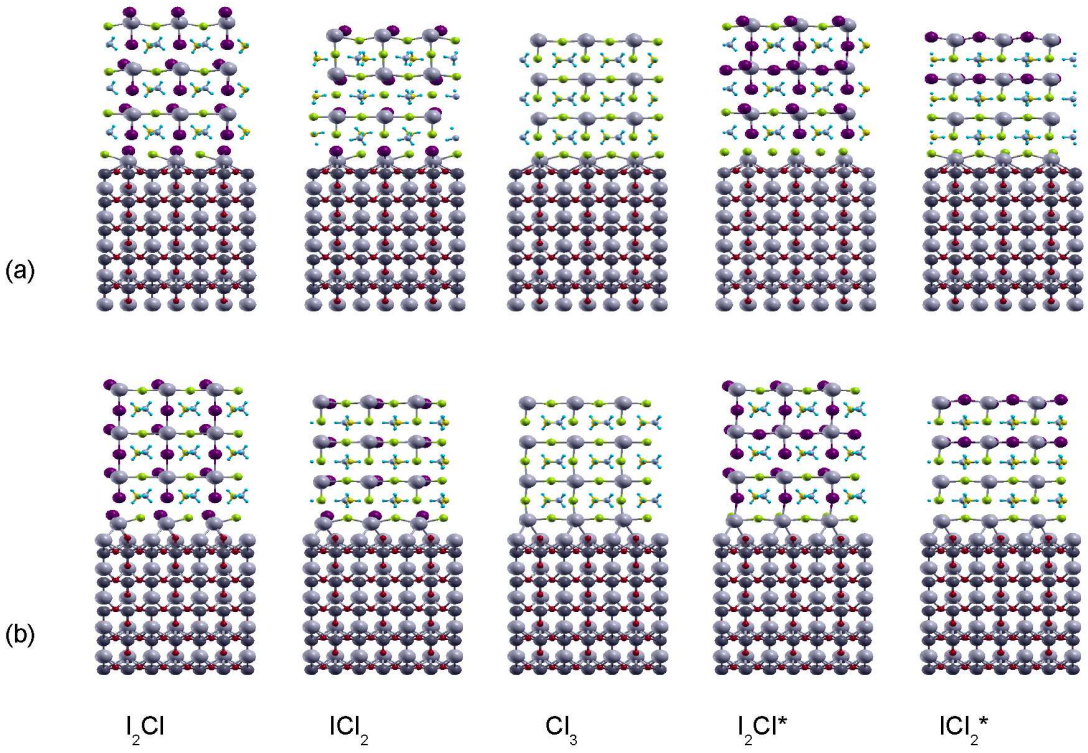

Figure 1: Structural models of the $MAPbI_{3-x}Cl_x$ / $PbTiO_3$ (001) heterostructures, x= 1,2 and 3. TiO_2 termination, (a), and PbO shifted termination, (b). Color code: Hydrogen light blue, carbon yellow, nitrogen dark blue, oxygen red, lead grey, titanium dark grey, iodine violet and chlorine yellow-green.

The data listed in Table 1 also show that there is a considerable mismatch between the in-plane lattice constants of the $MAPbX_3$, X= I and Cl, and that of the PTO conventional cell. Recently, Butler et al.[79] highlighted the importance of the lattice strain and lattice overlap at the interfaces on the device lifetime and stability, for materials with suitably matched band energies. In this study, in order to minimize the strains at the HP/PTO interface, the PTO (001) surface was oriented such as to expose a $\sqrt{2} \times \sqrt{2}$ (001) surface, (see Figure S3b in the

Supporting Information), with TiO_2 or PbO terminations, on-top which the $MAPbI_{3-x}Cl_x$ cells were placed. Although the in-plane lattice constants mismatch for $MAPbI_3$ is still about 14-15%, it decreases to less than 5% for at least one lattice constant as Cl gradually replaces I atoms. Thus, for the I_2Cl system, the mismatch along x-axis is 2.3% and 14.6% along the y-axis, for ICl_2 it is 5.1% along x and 2.3% along y, and for Cl_3 one obtains 2.9% along x and 2.2% along the y-axis. With an appropriate scaling of the HP layer in-plane lattice constants in order to simulate a coherent growth on the $\sqrt{2} \times \sqrt{2}$ PTO surface, the slabs, depicted in Figure 1, consist of three $MAPbI_{3-x}Cl_x$ unit cells - seven atomic layers - with $Pb(I,Cl)_2$ termination, deposited on the $PbTiO_3$ surface, consisting of five unit cells - ten atomic layers - negatively polarized (i.e. the polarization pointing downward from the interface). The thickness of the PTO layer is $\sim$ 2.1 nm, larger than the experimentally determined critical values when polarization becomes unstable.[37,45,80,81] Several slabs with the HP-MAX termination were also designed, see Figure S6, as suggested by one of the Reviewers, to highlight the changes in the electronic properties in their dependence on the HP termination at the interface. The vacuum size was set to $\sim$ 15 Å.

In the case of the PbO termination we performed calculations on slabs with two possible arrangements of the HP layer, in order to obtain more information on the effect of bonding at interfaces. The first one is characterized by a shift of the HP layer by one quarter of the PTO in-plane diagonal along the [110] direction, thus placing the Pb atoms in the HP interface layer over the O in the PbO layer. In the second arrangement the cells are unshifted and as a result one has lead on-top lead in the two layers at the interface. For the "PbO shifted" and TiO_2 terminations, two additional mixed halide slabs were considered, with chlorine preferentially distributed at the interface. For all the systems, the internal coordinates of the top three PTO unit cells from the interface were allowed to relax along the c-axis, while the internal coordinates of the HP layers were totally relaxed. The residual force on an atom was less than 0.03 eV/Å and the stress on the cell less than 17 kbar. In the following, we denote the slabs by the labels I_2Cl, ICl_2, Cl_3, I_2Cl* and ICl_2*, where the star symbol

indicates the Cl preferential distribution at the interface. Where not otherwise specified, we discuss the results obtained on slabs with $Pb(I,Cl)_2$ -terminated HP layer.

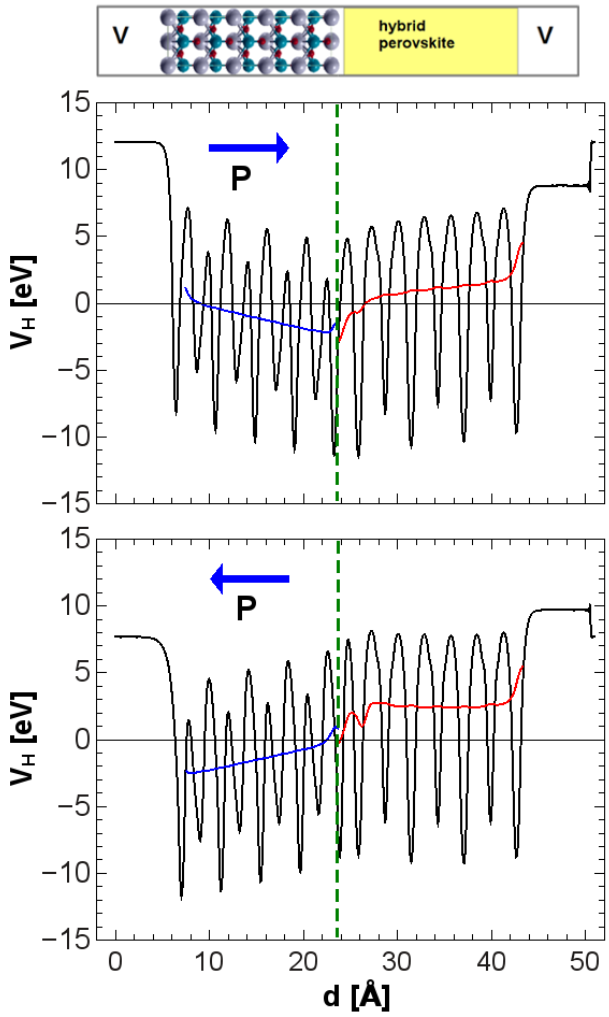

Figure 2: Illustrative plots of the planar (black) and macroscopic averages (blue for PTO and red for HP) of the Hartree potential, $\boldsymbol{V}_H$, along the z-axis of a model heterostructure, as a function of the direction of polarization in the $PbTiO_3$ layer. The green dashed line marks the position of the PTO-HP interface.

Figure 2 illustrates the Hartree potential, $\boldsymbol{V}_H$ variation along z-axis of the slabs in the presence of PTO polarization, $\boldsymbol{P}$. Referring to the two possible directions of $\boldsymbol{P}$, we chose the one with the polarization pointing from the interface to PTO. This choice favors the electron transport from the HP layer across the interface, to the lower Hartree potential in the PTO layer. The macroscopic averages of the Hartree potential, plotted in Figure 2, were

calculated for a slab with unrelaxed internal coordinates, using averaging windows equal to the c lattice constant of each material. Thus, the offset of the $\boldsymbol{V}_H$, as well as the magnitude of the electric dipole is independent of the interface geometry.[82,83]

3 Results and discussion

3.1 Structural results

The difference between the ionic radii of Cl and I determines a shrink of the slabs along the z-axis, see Figure 1, when increasing Cl concentration, consistent with the smaller Cl radius (1.81 Å) compared to that of I (2.16 Å), for six-fold coordination. The bond lengths across the three types of HP/PTO interfaces for HP-Pb(I,Cl)$_2$ termination are listed in Table 2, and those for HP-MA(I,Cl) termination in Table S1 (Supporting Information). Refering to the data displayed in Table 2, in the case of the TiO_2 surface termination and random I/Cl distribution, one notices that the Cl-Ti and I-Ti values in the present study, 2.8 Å and 3.3-3.4 Å, respectively, are larger than those calculated for the HP on rutile TiO_2 surface, 2.4 Å and 2.8 Å, respectively.[28] The Pb-O bond lengths are quite similar, in the 2.4-2.6 Å range. The Pb(HP)-Ti and Pb(HP)-O bond lengths slightly increase with chlorine concentration, whereas the X-O and X-Ti bonds show a decreasing trend. However, in the I_2Cl* and ICl_2* slabs, with chlorine at the interface, each of these bonds show two distinct values, one of them being notably larger than in the random I/Cl system. Also, in the case of the HP/PTO interfaces with both types of PbO terminations, the bond lengths show broader ranges of variation than in the case of the TiO_2 termination, and that correlates with the calculated surface rumpling, as discussed further. A comparison between the X-M bond lengths at the interface for the HP PbX_2 (Table 2) and MAX terminations (Table S1), shows that these are larger in the case of the MAX termination, due to the presence of the large MA molecule at the interface. Considering also the interface molecule dynamics, sustained by the MA correlations, one may assume that the PTO/HP-MAX interface is less stable than

the PTO/HP-PbX_2 one.

Table 2: Bond lengths at the interface hybrid perovskite-$PbTiO_3$ (001) surface, for the relaxed slabs. Note: A, B and C stand for TiO_2, PbO shifted and PbO terminations, respectively.

slab			d [Å]			
A	**Pb(HP)-Ti**	**Pb(HP)-O**	**Cl-O**	**I-O**	**Cl-Ti**	**I-Ti**
I_2Cl	3.26	2.43	3.19	3.61	2.80	3.37
ICl_2	3.26	2.43	3.11	3.49	2.78	3.27
Cl_3	3.31	2.52	3.13	–	2.74	–
I_2Cl*	3.26/3.30	2.43/2.49	3.29/3.39	> 4	2.96/3.08	> 4
ICl_2*	3.26/3.40	2.49/2.62	3.12/3.32	> 4	2.81/2.95	> 4
B	**Pb(HP)-Pb**	**Pb(HP)-O**	**Cl-O**	**I-O**	**Cl-Pb**	**I-Pb**
I_2Cl	3.09/3.20	2.65/3.09	3.52/3.57	3.83/ 3.96	3.80/3.88	> 4
ICl_2	3.03/3.17	2.74/2.97	3.38/3.58	3.67/ 3.82	3.65/3.85	3.76
Cl_3	3.37/3.48	3.23/3.25	3.31/3.67	–	3.59/3.78	–
I_2Cl*	3.37/3.42	3.18/3.23	3.45/3.54	> 4	3.68/3.71	> 4
ICl_2*	3.28/3.32	2.96/3.25	3.34/3.58	> 4	3.52/3.81	> 4
C						
I_2Cl	3.16/3.73	2.19	3.63	3.16	> 4	3.84
ICl_2	3.19	3.64	3.26	3.41	> 4	> 4
Cl_3	3.38	> 4	3.27/3.54	–	> 4	–

In the case of the (relaxed) slabs with HP PbX_2 termination layer we find that the MA dipoles align in the [110] direction, and show a weak trend to tilt with respect to z-axis only for the TiO_2 termination. In the case of the HP-MAX termination, which exposes the MA dipole directly to the PTO interface dipole, the present results show that: a) all MA dipoles lie between the [110] and [010] directions, with the MA dipole at interface also tilted toward z-axis, more for the TiO_2 and less for PbO shifted terminations; b) the MA dipoles in all the HP layers align between the [110] and [010] directions, with no trend to tilt toward z-axis, for the PTO-PbO termination. To sum up these observations, we suggest that the PTO-TiO_2 termination induces the strongest interface dipole, whereas the HP-PbX_2 termination screens the interface dipole at the MA site.

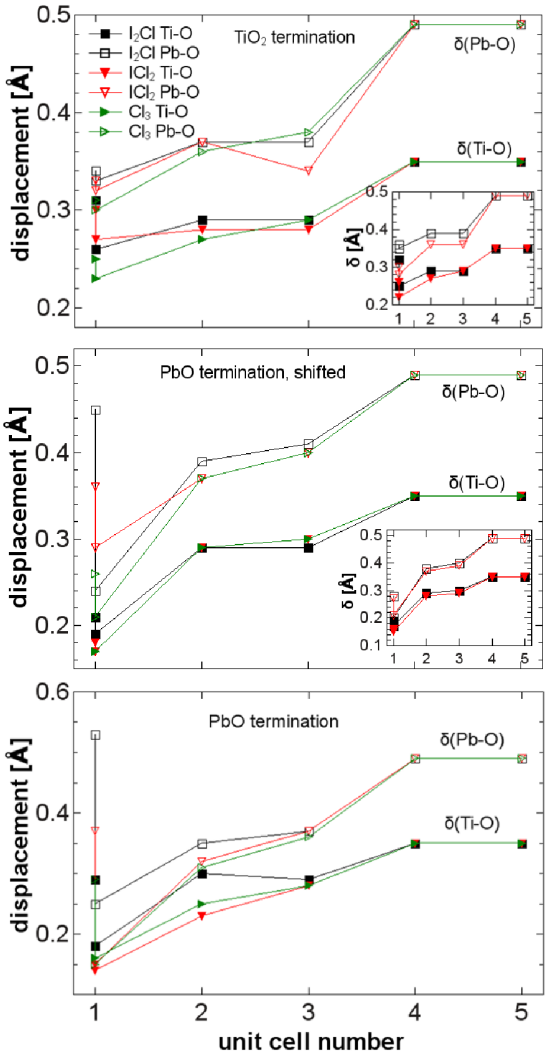

Figure 3: Ti-O (solid symbols) and Pb-O (hollow symbols) displacements along z-axis in the TiO_2 and PbO layers simulating the PTO surface, in the relaxed structures. The lines are guide to the eye. The unit cell number increases from the interface to the bottom of the PTO surface.

The Pb/Ti-O displacements, δ (Pb/Ti-O), along z-axis in the TiO_2 and PbO layers of the relaxed PTO surface were calculated using the expression δ (Pb/Ti-O) $= c_{slab} \cdot (z(O) - z(A))$ and are plotted in Figure 3 versus the unit cell number. The Pb-O displacements are larger than the Ti-O ones, and both sets of values decrease when advancing from the unrelaxed cells to the interface. As a result, the dipole moment of a PTO layer should also decrease toward the interface with respect to the value in the unrelaxed cells, in agreement with previous calculations.[84] The data collected in Figure 3 also reveal that no significant spread in the values of the Ti-O and Pb-O displacements exists within the relaxed layers, except in cell no.1 at the interface where δ(Ti-O) and δ(Pb-O) each take two different values. For the TiO_2 termination, the difference between the two δ(Ti-O) values is larger than that between δ(Pb-O) values, in the first cell from the interface; in the case of the PbO termination, the reverse situation occurs. This corresponds to a rumpling of the PTO surface which may account for the broad range of bond lengths determined in the HP/PbO interfaces. No qualitative difference between δ(Ti-O) and δ(Pb-O) variations along z-axis is observed for the two settings in the case of the PbO termination. Recently, Garrity et al.,[34] investigated by first principles the $PbTiO_3$ (001) surfaces, the effects of polarization on the electronic structure, stoichiometry, geometry, and reactivity. It was shown that the electronic and surface reconstruction mechanisms play a deterministic role on the bonding mechanism, binding energy, and the availability of binding sites. In the case of the complex interfaces of the heterostructures investigated in the present work, we will show that the junction characteristics have major effects on the charge density distribution, band alignment, and shape of the Hartree potential at the interface.

The model structures studied in this work allow to make a prediction on the preferential localization of chlorine in the heterostructures with mixed (Cl,I) compositions, based on energy considerations. The differences in total energy between calculations with the Cl preferentially distributed at the interface and (Cl,I) randomly distributed within the HP layer are plotted in Figure 4. These results suggest that the presence of chlorine at the inter-

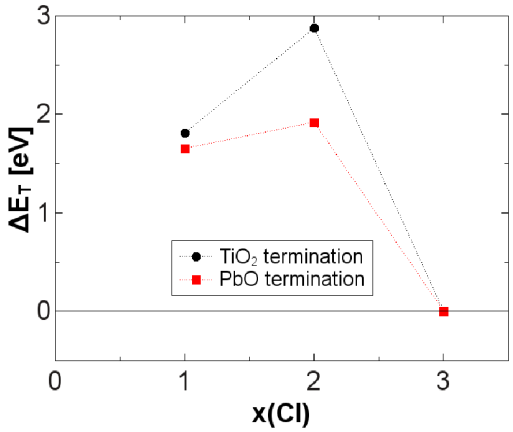

Figure 4: Total energy differences between calculations with Cl preferential distribution at the interface and (Cl,I) random distribution, for the systems with TiO_2 (black) and PbO (red) terminated PTO surfaces. The dotted lines are a guide to the eye.

face is not energetically favoured, for any of the PTO surface terminations, at least for the stoichiometries I_2Cl and ICl_2. Nevertheless, a more detailed study at low Cl concentration (x(Cl)$<$0.5), and taking into consideration possible effects, such as halide migration or formation of defects and complexes at interface, would be required to explain the experimental findings.[25]

3.2 Band alignment

The total and partial densities of states (PDOS) of the systems under study are plotted in Figure 5 for HP-PbX_2, and Figure S7 (Supporting Information) for the HP-MAX terminations. The valence-band maximum (VBM) is formed by Cl 3p, I 5p and O 2p states and the conduction-band minimum (CBM) has contributions from unoccupied Pb 6p and Ti 3d states (for details see the orbital projected DOS for $CH_3NH_3PbI_3$ in Figure S1 and for $PbTiO_3$ in Figure S2, in the Supporting Information).

In all cases, the states in the "pseudo" band gap, particularly for the TiO_2 termination, emerge mainly from Ti 3d, Pb 6p and O 2p, and this issue deserves a special comment. First, we have to highlight that in the plots in Figures 5 and S7, the PTO PDOS are taken from the "bulk-like" region of the layer simulating the ferroelectric surface, specifically the DOS

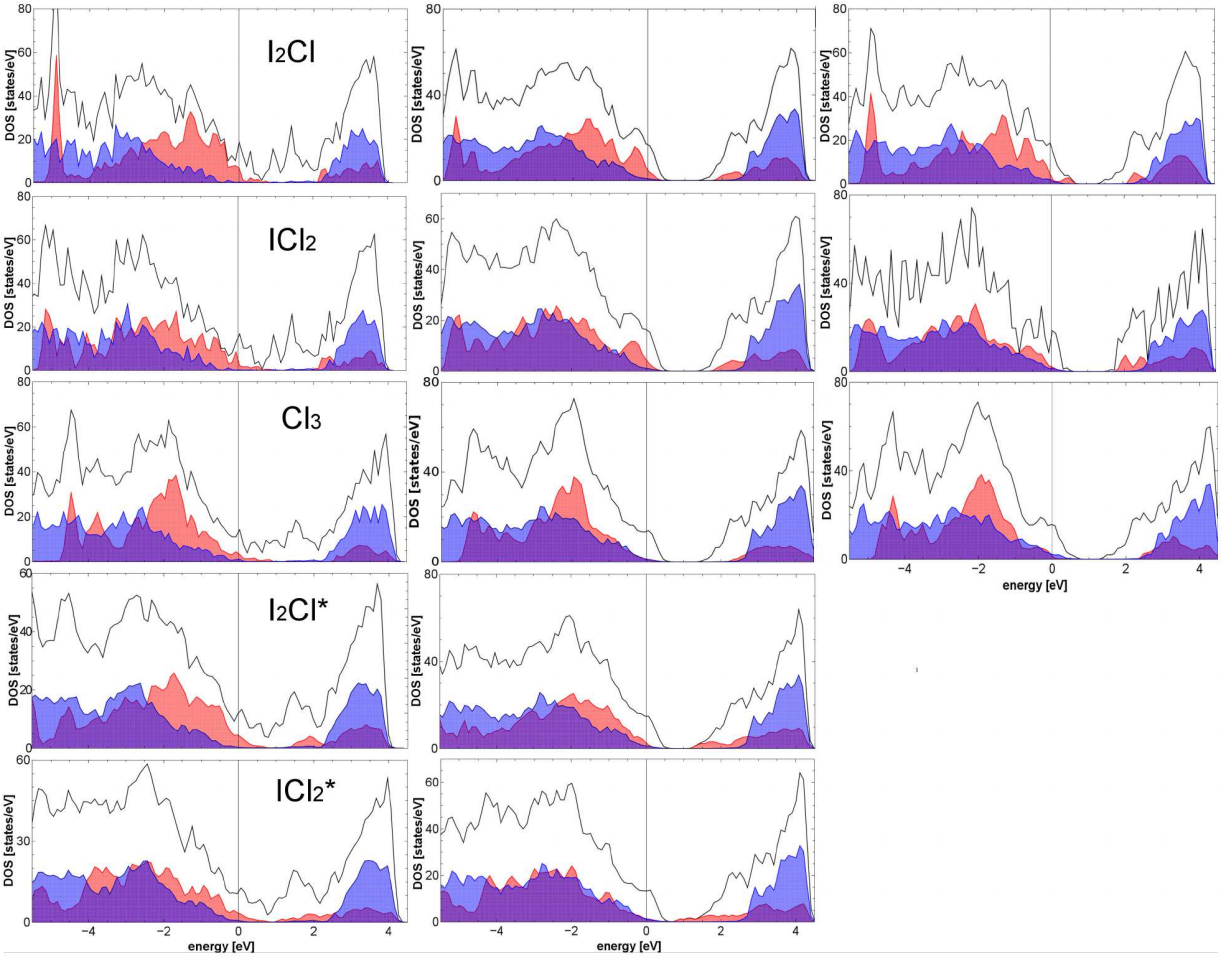

Figure 5: Total (black) and partial, hybrid perovskite (red) and PTO (blue) densities of states in $CH_3NH_3PbI_{3-x}Cl_x$ / PTO, x= 1, 2, and 3. TiO_2 termination, left column, PbO termination with shifted HP layers, middle column, and PbO termination, right column. In the case of the PTO PDOS, a "pseudo" band gap is observed, which characterizes the "bulk-like" region, see text for details. The Fermi energy is set at zero energy.

of the two inner PTO cells, and consequently they show a band gap; nevertheless, this gap is not observed in the total DOS. Therefore, in order to explain the origin of the band gap states, we have represented the contribution of each layer, TiO_2 and PbO, to the PTO total DOS, for, e.g., the case $MAPbCl_3$ on PTO (001), see Figures 6a and 6b. While the top PTO layers show an insulating behaviour, with the CBM at about 4 eV, advancing to the bottom layers a shift of the DOS to lower energy may be observed. As a result, the conduction band states in the bottom layers, extending from about -1 eV to higher energy (partially) overlap the position of the band gap of the top layers, and that is revealed in the total DOS plot, particularly for the TiO_2 surface termination. More insight into the band gap dependence on the position along the z-axis of the PTO slab and the spontaneous polarization direction is provided by the illustrative plots shown in Figure S4 in the Supporting Information, for the TiO_2 surface termination, with the polarization vector pointing downward (a), and upward (b). One may observe that the band edge positions also depend on the ferroelectric polarization direction in the PTO slab. We interpret these results as an electron depletion effect taking place in the layers next to the negative surface (bound) charge - thereof their insulating behaviour - and an electron enrichment effect in the layers next to the positive surface (bound) charge - which accounts for the Fermi level shift to the CB, and hence for the metallic behaviour. Also, in the DOS plots of the two topmost layers in Figures 6a and 6b, one may observe the presence of some features in the band gap, merged with the VBM, which may be associated with the bonding across the junction.

We used the DOS data plotted in Figures 5 and S7 to draw tentative schemes of the band alignment in these heterostructures, see Figures 7 and S8. Firstly, one may observe that the HP band gaps increase in the sequence I_2Cl, ICl_2, Cl_3, with the lattice constants decreasing as a result of the bigger iodine atom, with higher occupied orbitals being replaced by the smaller chlorine atom, with lower occupied orbitals. Then, referring to Figure 7, the TiO_2 termination results in higher HP bands and the PbO termination results in higher PTO bands. This may be used to switch the polarity of the interface by control of the PTO

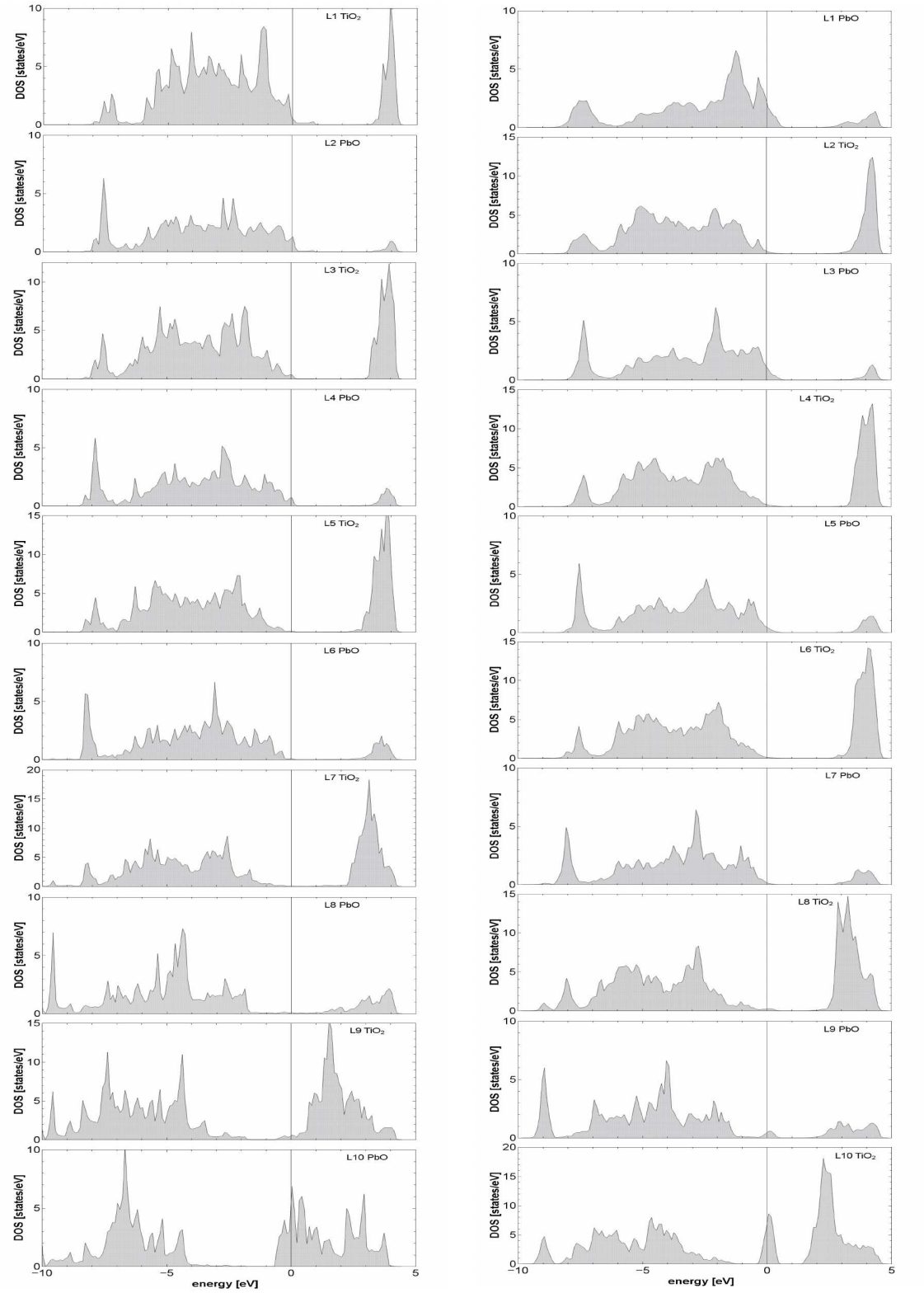

Figure 6: PTO layer-resolved partial DOS for the Cl_3 slabs with TiO_2 termination (a), and PbO shifted termination, (b). The Fermi energy is set at zero energy.

surface termination: one can combine control of the termination in PTO, with control of stoichiometry in HP to achieve a Schottky or a perfect Ohmic contact. Also, generally, the introduction of I shifts the HP valence band edge to higher values (relative to the PTO), which makes sense given the higher p-orbital energy in I than in Cl.

The band offsets are favourable for electron transport only for the slabs with TiO_2 termination, and particularly for the Cl_3 heterostructure. In the I_2Cl and ICl_2 systems the CBM of the HP is slightly below that in the PTO and a reversed, favourable offset could eventually be induced by tuning the Cl concentration. One may also assume that an adequate band alignment of the CBM and VBM for electron transfer could take place in the hypothetical $MAPbI_3$/ PTO (001) heterostructure, provided that this one could experimentally be engineered. The CB offsets in the series with PbO termination are obviously unfavourable to electron transfer from the hybrid perovskite to the PTO material. Cl redistribution at the interface lowers the CBM of the HP in all cases, this effect being more pronounced for the PbO termination. No significant qualitative difference may be observed between the band alignment schemes of the two cases considered for the PbO termination, see Figures 7b and 7c. However, a more detailed band alignment scheme may be obtained using, e.g., the data plotted in Figure 6 left panel for the Cl_3 slab with TiO_2 terminated PTO, as depicted in Figure 8. Due to the internal electric field, the VB and CB edges within the PTO layer are position dependent in the electron path to the collecting electrode. We suggest that this property may be used to establish a relationship between optimal carriers transport and the thickness of the ferroelectric layer in a practical device.

An examination of the band structure plots, drawn in Figure S5 in the Supporting Information, reveals that, apparently, the middle and right columns corresponding to the PbO shift and PbO terminations, respectively, show band gaps. However, at a closer look, these plots show that a few bands in the valence band cross the nearby Fermi level (set at zero energy) at X, and particularly at M high symmetry k-points, whereas at the Γ point the band structure is similar to that of a p-type semiconductor. Actually, it is due to the non-zero

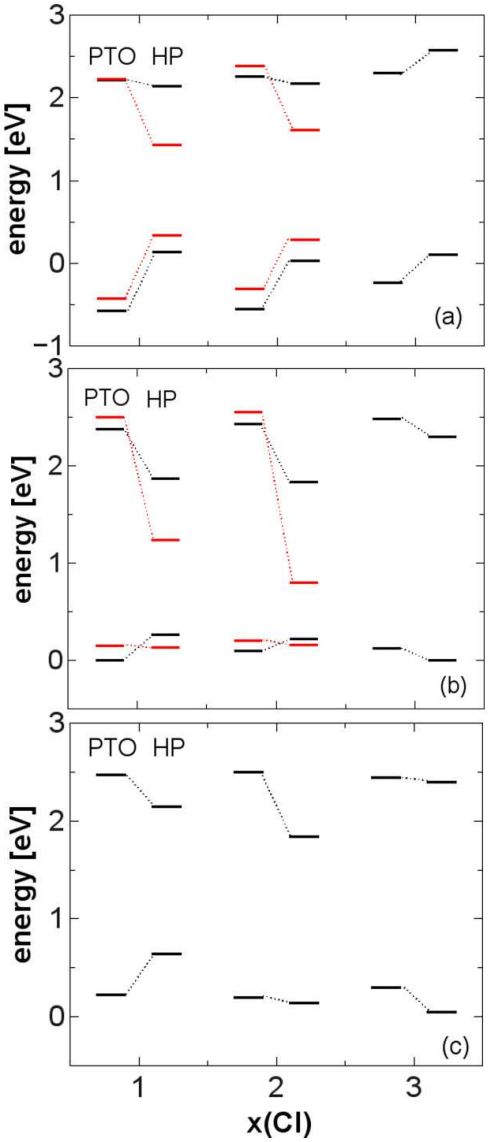

Figure 7: Band alignment schemes for the TiO_2 (a), PbO shifted (b), and PbO (c) surface terminations. The red lines mark the VBM and CBM positions when the Cl ions within the hybrid perovskite (HP) layer are preferentially distributed at interface.

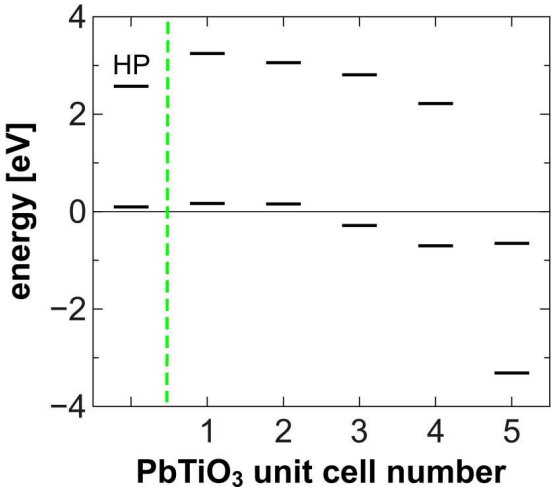

Figure 8: Dependence of the $PbTiO_3$ band gap on the unit cell position from the interface (marked with a green dashed line), for $CH_3NH_3PbCl_3/PbTiO_3$ (001). The VBM and CBM levels of the hybrid perovskite are also indicated.

density of states at the Fermi energy at the X and M points that we refer to these materials as showing a metallic character, which may also be observed in the total DOS.

3.3 Charge density, Hartree potential and ionization potential

In a solar cell, it is required that the photogenerated charge in the light absorber to be rapidly separated and transmitted to the electrodes. In zero applied electric field, the carriers move under the action of a potential which is mainly determined by the characteristics of the interfaces and the charge density distribution in the device. Therefore, knowledge of both quantities is of utmost importance in order to optimize the cell design for high energetic efficiency. The macroscopic averages of charge densities and their differences in the systems under investigations are plotted in Figures 9 and 10.

For both PTO terminations, the macroscopically averaged charge density in the PTO is about three times larger than that in the HP, as evidenced in Figures 9a and 10a. The electronic transition region at the interface extends over a distance of about 10 Å. The effect of (I,Cl) composition on charge density distribution is revealed in Figures 9b and 10b. When varying Cl concentration, no significant differences in the amplitude of charge density oscil-

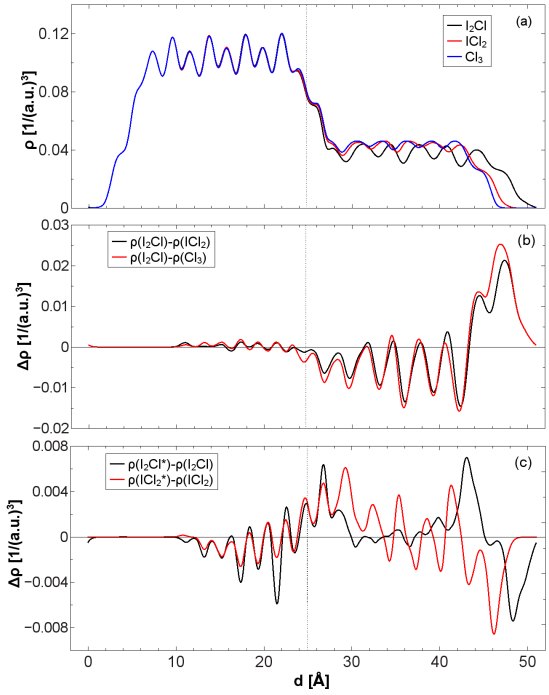

Figure 9: Macroscopic average of charge density along the z-axis, (a), and charge density differences to reveal the effects of Cl concentration, (b), and (I,Cl) distribution, (c), for TiO_2 termination.

lations are observed for a given PTO surface termination. However, an obvious difference between their augmentation from the interface into the PTO layer, much larger for the TiO_2 than for the PbO termination, may be remarked. Having in view that, previously, the extension of charge density oscillations from the HP into the TiO_2 layer has been associated with a favourable effect on the electron transport across the interface,[28] we suggest that a simmilar effect may take place in the HP/PTO interfaces with TiO_2-terminated surface. Figures 9c and 10c display the differences between the macroscopic averages of charge density for the I_2Cl and ICl_2 slabs, with random (Cl,I) and preferential Cl distributions. The dependences show that the presence of Cl at the interface promotes an enhancement of the charge density oscillations into the PTO, more extended in the case of the TiO_2 termination than for the PbO one, in agreement with previous calculations.[28] We suggest that i) the shorter Cl-Ti/Pb bonds comparing to I-Ti/Pb, see Table 2 for the TiO_2 and PbO terminations, and ii) the larger Pauli electronegativity of chlorine (3.0) comparing to that of iodine (2.5) determine

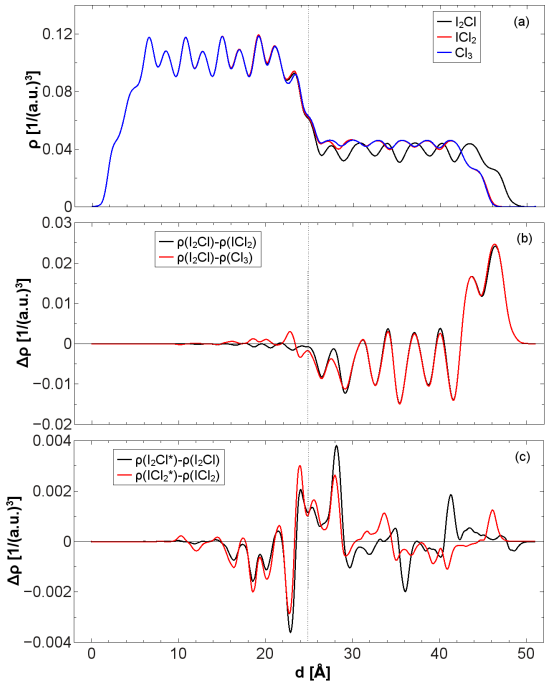

Figure 10: Macroscopic average of charge density along the z-axis, (a), and charge density differences to reveal the effects of Cl concentration, (b), and (I,Cl) distribution, (c), for PbO termination.

the significant charge redistribution at the HP/PTO interface with respect to less or no interfacial chlorine. In the case of HP-MAX termination, Cl-Ti/Pb bond lengths are close or even larger than I-Ti/Pb bonds, see Table S1. Since a significant change of the charge distribution takes also place near the HP/PTO interface, see Figures S9b and S10b, the effect may be associated with both the larger chlorine electronegativity as well as with an enhanced interface dipol.

The planar averages and the macroscopic averages of the Hartree potential are plotted in Figure 11. After applying the dipole correction, the potential is constant in the vacuum region albeit with different values on the two sides of the heterostructures. This is a consequence of the presence of internal dipoles, smaller in the HP and bigger in the PTO layers, as more clearly revealed by the slopes of the $\boldsymbol{V}_H$ macroscopic averages in the PTO and HP. Also, the macroscopic averages in the HP layers look less smooth than those in the PTO due to MA molecules orienting in different directions. We highlight the influence of an interface dipole,

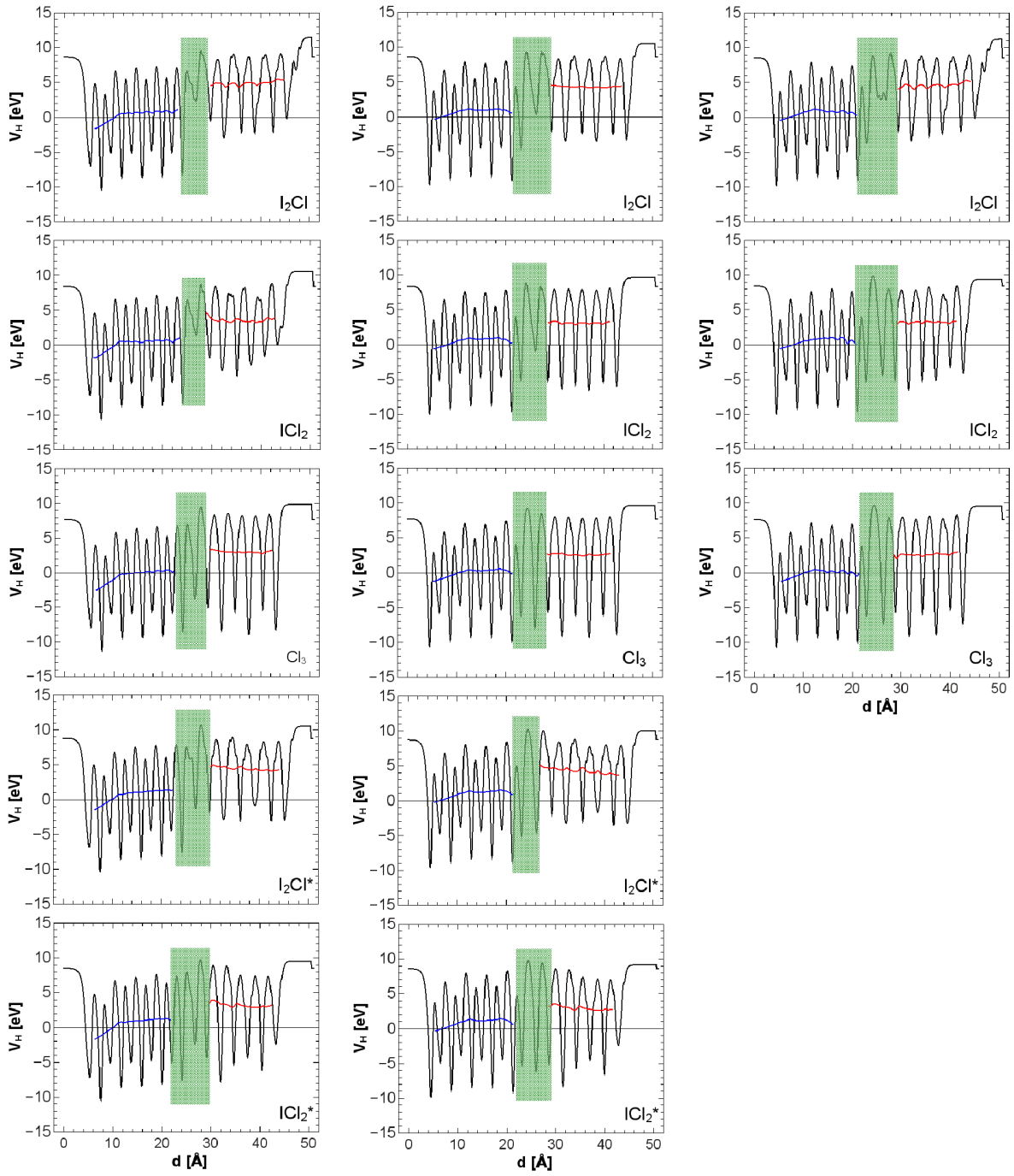

Figure 11: Planar averages of the Hartree potential (black) and the macroscopic averages (blue line for PTO and red line for HP), along the z-axis of the heterostructures: TiO_2 termination, left column; PbO shifted termination, middle column; PbO termination, right columnl. The area in green marks an estimated width of the PTO/HP electronic interface.

which is evident from the offset of the $\boldsymbol{V}_H$ on each side of the junction. Generally, this offset decreases as the Cl concentration increases. It is interesting to remark that bringing Cl at the interface, the case of the I_2Cl* and ICl_2* slabs, has the effect of increasing the potential on the HP side of the junction, which is in qualitative agreement with the effect on MA dipoles orienting.[28]

The area marked in green at the HP/PTO interface in Figure 11 is intended to provide a sense of the spatial extension along z-axis of perturbed $\boldsymbol{V}_H$, associated with an "electronic" interface. The limits along z-axis were estimated mainly by a 10 % variation in $\boldsymbol{V}_H$ with respect to the average value in the relaxed bulk when approaching the interface from the PTO (or the HP) side of the heterostructure. However, a visual estimate was prefered when large oscilations in $\boldsymbol{V}_H$ develop near the interface.

Table 3: Potential data (in eV): vacuum potential on the PTO side, $\boldsymbol{V}_{v,PTO}$, vacuum potential on the HP side, $\boldsymbol{V}_{v,HP}$, their difference, $\Delta \boldsymbol{V}_v$, ionization potential on the PTO side, $\boldsymbol{IP}_{PTO}$, ionization potential on the HP side, $\boldsymbol{IP}_{HP}$, valence band maximum, VBM_{HP} and Fermi energy, $\boldsymbol{E}_F$. Note: A, B and C stand for TiO_2, PbO shifted and PbO terminations, respectively.

A	$\boldsymbol{V}_{v,PTO}$	$\boldsymbol{V}_{v,HP}$	$\Delta \boldsymbol{V}_v$	$\boldsymbol{IP}_{PTO}$	$\boldsymbol{IP}_{HP}$	VBM_{HP}	$\boldsymbol{E}_F$
I_2Cl	8.68	11.45	2.78	3.39	11.33	0.12	5.29
ICl_2	8.40	10.58	2.18	3.35	10.48	0.10	5.05
Cl_3	7.68	9.80	2.12	3.32	9.60	0.20	4.36
I_2Cl*	8.81	10.55	1.74	3.40	9.81	0.74	5.41
ICl_2*	8.55	9.52	0.97	3.42	8.75	0.77	5.13
B							
I_2Cl	8.64	10.60	1.96	3.59	10.1	0.30	5.05
ICl_2	8.39	9.66	1.27	3.58	9.21	0.27	4.81
Cl_3	7.69	9.60	1.91	3.55	9.08	0.07	4.14
I_2Cl*	8.77	10.04	1.27	3.64	9.52	0.13	5.13
ICl_2*	8.64	9.22	0.57	3.66	8.69	0.16	4.98
C							
I_2Cl	8.64	11.31	2.67	3.65	10.64	0.64	4.99
ICl_2	8.39	9.41	1.02	3.53	9.03	0.14	4.86
Cl_3	7.69	9.60	1.91	3.58	8.93	0.05	4.11

The values of the Hartree potential in vacuum, the Fermi level position, the valence band maximum for the hybrid perovskite and the ionization potential, IP, calculated on each side of

the heterostructure are collected in Table 3. Since the PTO side shows a metallic behaviour, the $\boldsymbol{IP}_{PTO}$ equals the work function and the values are derived by subtracting the Fermi energy from the value in vacuum. The HP layers show insulating behaviour and therefore the $\boldsymbol{IP}_{HP}$ is determined as the difference between the HOMO energy (VBM) and the value in vacuum. The fact that $\boldsymbol{IP}_{PTO}$ and $\boldsymbol{IP}_{HP}$ are significantly different, as a consequence of both the built-in potential due to the ferroelectric PTO and the different frontier orbital characters of the materials on either side of the interface, should lead to a low barrier to electron collection at such interfaces and a reduced contact resistance overall.

Finally, it is worth to note that the Hartree potential and ionization potential results displayed in Figure S11 and Table S2, respectively, for the PTO/HP-MAX systems, are qualitatively similar to the corresponding data for the PTO/HP-PbX_2 systems.

4 Conclusions

We studied by DFT calculations various heterostructures consisting of $CH_3NH_3PbI_{3-x}Cl_x$ layers deposited on ferroelectric $PbTiO_3$ (001) surfaces, in order to theoretically assess their potential for use in photovoltaic devices, aiming to improved charge separation and transport properties in comparison with the HP/TiO_2 systems.

Firstly, we outline the conclusions for the PTO/HP-PbX_2 interfaces. As a result of the relaxation process, we find that the Pb-O and Ti-O displacements decrease toward the interface with the HP, consistent with a decrease of the PTO polarization with respect to the value in the bulk. One notices that there are no qualitative differences between the two different settings used for the systems with PbO termination, as also revealed by the bond lengths. Since the presence of the ferroelectric surface seems to have no influence on aligning the MA dipoles, during the atomic relaxation process, we suggest that the effects associated with dipole dynamics and disorder may persist in the HP/PTO heterostructures. In particular, the interface polarization may prevent the migration of the halogen ions toward

the hole transporter, and that may possibly reduce the hysteresis of the I-V curves.

Using the Cl_3 slabs as an example, we show that the layer resolved PTO DOS shift to lower energy with the distance from the interface, due to the internal electric field, and determines the appearance of a density of states in the band gap of total DOS. A relatively smaller contribution from the HP-PTO bonding at the interface sums up to give the density of states observed in the "band gap" of the total DOS of each system.

The band alignment scheme obtained with the PTO contribution to DOS taken only from the bulk-like region underscores the fact that the electron transfer from HP to PTO may occur only for the TiO_2 termination and random (I,Cl) distribution. Using as an illustrative case the Cl_3 slab with TiO_2 termination, we show a more detailed image of the band alignment pecularity in these systems. We suggest that, at the HP/PTO interface: i) by combining the control of the termination layer in the PTO, with the control of stoichiometry in HP, one may achieve a Schottky or a perfect Ohmic contact; ii) the present results for the two mixed (I,Cl) compositions predict that Cl preferential distribution at the interface lowers the CBM of the HP relative to that of the PTO, thus impeding the electron transfer, in all cases; iii) a favourable band alignment for electron transfer could also be effective in a lattice constant matched MAPbI3:PTO (001) heterostructure.

We find that increasing chlorine concentration increases the electronic potential on the HP side and promotes charge density oscillations into the PTO layer, similarly to the case of HP layers on TiO_2 surfaces. These oscillations have larger amplitude and develop more into the PTO layer for the TiO_2 termination than for the PbO termination. Thus, while one may expect an improvement in charge transport, and consequently in the PCE, in the mixed (I,Cl) systems, the present data emphasize that Cl concentration and distribution should be finely tuned, due to their repercussion on the band alignment details. A feature also found in the HP-TiO_2 case is the diminished valence band offset as the concentration of chlorine is increased, which can be observed by comparing Figure 7 of the present paper with Figure 5 in Nemnes et al..[28] Accordingly, the hole blocking capacity of the electron

transport layers may be lowered. However, in contrast to the HP-TiO_2 case, a significant difference appears due to the ferroelectric properties of PTO, which leads to a position dependent energy diagram (Figure 8). This aspect suggests an enhanced electron collection due to a properly oriented internal electric field. In this context, a larger HP gap tuned by chlorine concentration may increase the band offset or reduce the potential spike in the conduction band. Therefore, a certain amount of chlorine-based halide perovskite present near the interface may be optimal, as also indicated in.[28] Finally, our results also highlight that the use of FE PTO electron transporter layer results in a significant asymmetry between the ionization potential values at each side of the HP/PTO heterostructures, with $\boldsymbol{IP}_{PTO}$ significantly smaller than $\boldsymbol{IP}_{HP}$, which is a favourable situation for charge separation and transfer across a photovoltaic device.

As regards the PTO/HP-MAX interfaces, some additional concluding remarks may also be drawn. Thus, the longer X-M bonds and the interface molecule dynamics point to these systems as potentially less stable than the PTO/HP-PbX_2 ones. We suggest that the interfacial chlorine produces a significant charge redistribution near the PTO/HP-MAX interface due to its larger electronegativity than that of iodine, and the presence of an enhanced interface dipol moment. Since the ionization potential results are in qualitative agreement with the corresponding data for the PTO/HP-PbX_2 systems. we suggest that the electrical performance of a practical solar cell may not be sensitive to the HP PbX_2 or MAX interfacial layer at the PTO (001) surface.

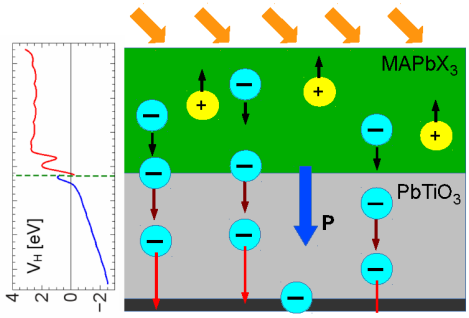

Supporting Information Available

GGA PBEsol PDOS, band structure and unit cell of 'pseudo-cubic' $MAPbI_3$. GGA+U PBEsol PDOS and band structure of tetragonal $PbTiO_3$, and detail of (001) surface orientation. PTO (001) layer-resolved PDOS for the $MAPbCl_3$/PTO-TiO_2 slab versus the polarization direction. Band structures of HP-PbX_2/PTO interfaces. Structural models, bond lengths, PDOS, band alignment schemes, Cl concentration and (I,Cl) distribution effect on the macroscopic averages of charge density, planar and macroscopic averages along z-axis of the Hartree potential, potential data, lattice vectors and atomic coordinates of HP-MAX/PTO heterostructures (PDF).

This material is available free of charge via the Internet at http://pubs.acs.org/.

Acknowledgement

The research leading to these results has received funding from EEA Financial Mechanism 2009-2014 under the project contract no 8SEE/30.06.2014. N.P., L.F., L.P. and I.P. gratefully acknowledge partial support within NIMP "Core Program 2016-2017, Project 1". N.P. and L.F. also acknowledge funding from the project PN-II-RU-TE-2012-3-0320 (Contract No. 11).

References

(1) Jung, H. S.; Park, N.-G. Perovskite Solar Cells: From Materials to Devices. *Small* **2015**, *11*, 10–25.

(2) Chen, Q.; De Marco, N.; Yang, Y. M.; Song, T.-B.; Chen, C.-C.; Zhao, H.; Hong, Z.; Zhou, H.; Yang, Y. Under the Spotlight: The Organic–Inorganic Hybrid Halide Perovskite for Optoelectronic Applications. *Nano Today* **2015**, *10*, 355–396.

(3) Sum, T. C.; Chen, S.; Xing, G.; Liu, X.; Wu, B. Energetics and Dynamics in Organic–

Inorganic Halide Perovskite Photovoltaics and Light Emitters. *Nanotechnology* **2015**, *26*, 342001.

(4) Frost, J. M.; Butler, K. T.; Brivio, F.; Hendon, C. H.; Van Schilfgaarde, M.; Walsh, A. Atomistic Origins of High-Performance in Hybrid Halide Perovskite Solar Cells. *Nano Lett.* **2014**, *14*, 2584–2590.

(5) Egger, D. A.; Rappe, A. M.; Kronik, L. Hybrid Organic–Inorganic Perovskites on the Move. *Acc. Chem. Res.* **2016**, *49*, 573–581.

(6) Mosconi, E.; Amat, A.; Nazeeruddin, M. K.; Grätzel, M.; De Angelis, F. First-Principles Modeling of Mixed Halide Organometal Perovskites for Photovoltaic Applications. *J. Phys. Chem. C* **2013**, *117*, 13902–13913.

(7) Eames, C.; Frost, J. M.; Barnes, P. R.; O'Regan, B. C.; Walsh, A.; Islam, M. S. Ionic Transport in Hybrid Lead Iodide Perovskite Solar Cells. *Nature Communications* **2015**, *6*, 7497.

(8) Frost, J. M.; Walsh, A. What is Moving in Hybrid Halide Perovskite Solar Cells ? *Acc. Chem. Res.* **2016**, *49*, 528–535.

(9) Frost, J. M.; Butler, K. T.; Walsh, A. Molecular Ferroelectric Contributions to Anomalous Hysteresis in Hybrid Perovskite Solar Cells. *Apl Materials* **2014**, *2*, 081506.

(10) Goehry, C.; Nemnes, G. A.; Manolescu, A. Collective Behavior of Molecular Dipoles in $CH_3NH_3PbI_3$. *J. Phys. Chem. C* **2015**, *119*, 19674–19680.

(11) Butler, K. T.; Frost, J. M.; Walsh, A. Ferroelectric Materials for Solar Energy Conversion: Photoferroics Revisited. *Energy Environ. Sci.* **2015**, *8*, 838–848.

(12) Johnston, M. B.; Herz, L. M. Hybrid Perovskites for Photovoltaics: Charge-Carrier Recombination, Diffusion, and Radiative Efficiencies. *Acc. Chem. Res.* **2015**, *49*, 146–154.

(13) Galkowski, K.; Mitioglu, A.; Miyata, A.; Plochocka, P.; Portugall, O.; Eperon, G. E.; Wang, J. T.-W.; Stergiopoulos, T.; Stranks, S. D.; Snaith, H. J. et al. Determination of the Exciton Binding Energy and Effective Masses for Methylammonium and Formamidinium Lead Tri-halide Perovskite Semiconductors. *Energy Environ. Sci.* **2016**, *9*, 962–970.

(14) Wright, A. D.; Verdi, C.; Milot, R. L.; Eperon, G. E.; Pérez-Osorio, M. A.; Snaith, H. J.; Giustino, F.; Johnston, M. B.; Herz, L. M. Electron-Phonon Coupling in Hybrid Lead Halide Perovskites. *Nature Communications* **2016**, *7*, 1–9.

(15) Poglitsch, A.; Weber, D. Dynamic Disorder in Methylammoniumtrihalogenoplumbates (II) Observed by Millimeter-Wave Spectroscopy. *J. Chem. Phys.* **1987**, *87*, 6373–6378.

(16) Brivio, F.; Walker, A. B.; Walsh, A. Structural and Electronic Properties of Hybrid Perovskites for High-Efficiency Thin-Film Photovoltaics from First-Principles. *APL Materials* **2013**, *1*, 042111.

(17) Crystal Structures of Hybrid Perovskites Are Not 0K. http://tinyurl.com/hybrid-perovskites-not-0k, accessed April 8, 2017.

(18) Baikie, T.; Fang, Y.; Kadro, J. M.; Schreyer, M.; Wei, F.; Mhaisalkar, S. G.; Grätzel, M.; White, T. J. Synthesis and Crystal Chemistry of the Hybrid Perovskite $(CH_3NH_3)PbI_3$ for Solid-State Sensitised Solar Cell Applications. *J. Mat. Chem. A* **2013**, *1*, 5628–5641.

(19) Lee, J.-H.; Bristowe, N. C.; Lee, J. H.; Lee, S.-H.; Bristowe, P. D.; Cheetham, A. K.; Jang, H. M. Resolving the Physical Origin of Octahedral Tilting in Halide Perovskites. *Chem. Mater.* **2016**, *28*, 4259–4266.

(20) Loi, M. A.; Hummelen, J. C. Hybrid Solar Cells: Perovskites Under the Sun. *Nature Materials* **2013**, *12*, 1087–1089.

(21) Colella, S.; Mosconi, E.; Fedeli, P.; Listorti, A.; Gazza, F.; Orlandi, F.; Ferro, P.; Besagni, T.; Rizzo, A.; Calestani, G. et al. $MAPbI_{3-x}Cl_x$ Mixed Halide Perovskite for Hybrid Solar Cells: The Role of Chloride as Dopant on the Transport and Structural Properties. *Chem. Mater.* **2013**, *25*, 4613–4618.

(22) Colella, S.; Mosconi, E.; Pellegrino, G.; Alberti, A.; Guerra, V. L.; Masi, S.; Listorti, A.; Rizzo, A.; Condorelli, G. G.; De Angelis, F. et al. Elusive Presence of Chloride in Mixed Halide Perovskite Solar Cells. *J. Phys. Chem. Lett.* **2014**, *5*, 3532–3538.

(23) Song, D.-h.; Heo, J. H.; Han, H. J.; You, M. S.; Im, S. H. Reproducible Formation of Uniform $CH_3NH_3PbI_{3-x}Cl_x$ Mixed Halide Perovskite Film by Separation of the Powder Formation and Spin-Coating Process. *Journal of Power Sources* **2016**, *310*, 130–136.

(24) Bae, D.; Palmstrom, A.; Roelofs, K.; Mei, B.; Chorkendorff, I.; Bent, S. F.; Vesborg, P. C. Tailoring Mixed-Halide, Wide-Gap Perovskites via Multistep Conversion Process. *ACS Applied Materials & Interfaces* **2016**, *8*, 14301–14306.

(25) Edri, E.; Kirmayer, S.; Kulbak, M.; Hodes, G.; Cahen, D. Chloride Inclusion and Hole Transport Material Doping to Improve Methyl Ammonium Lead Bromide Perovskite-Based High Open-Circuit Voltage Solar Cells. *J. Phys. Chem. Lett.* **2014**, *5*, 429–433.

(26) Lee, M. M.; Teuscher, J.; Miyasaka, T.; Murakami, T. N.; Snaith, H. J. Efficient Hybrid Solar Cells Based on Meso-Superstructured Organometal Halide Perovskites. *Science* **2012**, *338*, 643–647.

(27) Mosconi, E.; Ronca, E.; De Angelis, F. First-Principles Investigation of the TiO_2/Organohalide Perovskites Interface: The Role of Interfacial Chlorine. *J. Phys. Chem. Lett.* **2014**, *5*, 2619–2625.

(28) Nemnes, G.; Goehry, C.; Mitran, T.; Nicolaev, A.; Ion, L.; Antohe, S.; Plugaru, N.; Manolescu, A. Band Alignment and Charge Transfer in Rutile-TiO_2/$CH_3NH_3PbI_{3-x}Cl_x$ Interfaces. *Phys. Chem. Chem. Phys.* **2015**, *17*, 30417–30423.

(29) Yang, G.; Tao, H.; Qin, P.; Ke, W.; Fang, G. Recent Progress in Electron Transport Layers for Efficient Perovskite Solar Cells. *J. Mat. Chem. A* **2016**, *4*, 3970–3990.

(30) Ibbetson, J.; Fini, P.; Ness, K.; DenBaars, S.; Speck, J.; Mishra, U. Polarization Effects, Surface States, and the Source of Electrons in AlGaN/GaN Heterostructure Field Effect Transistors. *Appl. Phys. Lett.* **2000**, *77*, 250–252.

(31) Kim, Y.-M.; Morozovska, A.; Eliseev, E.; Oxley, M. P.; Mishra, R.; Selbach, S. M.; Grande, T.; Pantelides, S.; Kalinin, S. V.; Borisevich, A. Y. Direct Observation of Ferroelectric Field Effect and Vacancy-Controlled Screening at the $BiFeO_3/La_xSr_{1-x}MnO_3$ Interface. *Nature Materials* **2014**, *13*, 1019–1025.

(32) Freysoldt, C.; Rinke, P.; Scheffler, M. Controlling Polarization at Insulating Surfaces: Quasiparticle Calculations for Molecules Adsorbed on Insulator Films. *Phys. Rev. Lett.* **2009**, *103*, 056803.

(33) Kraya, L. Y.; Kraya, R. Polarization Dependence of Molecular Adsorption on Ferroelectrics. *Acta Cryst. B* **2013**, *69*, 105–109.

(34) Garrity, K.; Kakekhani, A.; Kolpak, A.; Ismail-Beigi, S. Ferroelectric Surface Chemistry: First-Principles Study of the $PbTiO_3$ Surface. *Phys. Rev. B* **2013**, *88*, 045401.

(35) Alawode, B. O.; Kolpak, A. M. $PbTiO_3$ (001) Capped with ZnO $(11\bar{2}0)$: An Ab Initio Study of Effect of Substrate Polarization on Interface Composition and CO_2 Dissociation. *J. Phys. Chem. Lett.* **2016**, *7*, 1310–1314.

(36) Baeumer, C.; Saldana-Greco, D.; Martirez, J. M. P.; Rappe, A. M.; Shim, M.; Martin, L. W. Ferroelectrically Driven Spatial Carrier Density Modulation in Graphene. *Nature Communications* **2015**, *6*, 6136.

(37) Pintilie, L.; Ghica, C.; Teodorescu, C. M.; Pintilie, I.; Chirila, C.; Pasuk, I.; Trupina, L.;

Hrib, L.; Boni, A. G.; Apostol, N. G. et al. Polarization Induced Self-Doping in Epitaxial $Pb(Zr_0.20Ti_0.80)O_3$ Thin Films. *Sci. Rep.* **2015**, *5*, 14974.

(38) Scott, J. F. *Ferroelectric Memories*; Springer-Verlag Berlin Heidelberg, 2000; Vol. 3.

(39) Fridkin, V. M. Critical Size in Ferroelectric Nanostructures. *Physics-Uspekhi* **2006**, *49*, 193.

(40) Fridkin, V.; Ducharme, S. *Ferroelectricity at the Nanoscale*; Springer, 2014; pp 1–9.

(41) Shimada, T.; Wang, X.; Kondo, Y.; Kitamura, T. Absence of Ferroelectric Critical Size in Ultrathin $PbTiO_3$ Nanotubes: A Density-Functional Theory Study. *Phys. Rev. Lett.* **2012**, *108*, 067601.

(42) Alexe, M.; Gruverman, A. *Nanoscale Characterisation of Ferroelectric Materials: Scanning Probe Microscopy Approach*; Springer Science & Business Media, 2013.

(43) Rabe, K. M.; Ahn, C. H.; Triscone, J.-M. *Physics of Ferroelectrics: A Modern Perspective*; Springer Science & Business Media, 2007; Vol. 105.

(44) Hong, S. *Nanoscale Phenomena in Ferroelectric Thin Films*; Springer Science & Business Media, 2004.

(45) Junquera, J.; Ghosez, P. Critical Thickness for Ferroelectricity in Perovskite Ultrathin Films. *Nature* **2003**, *422*, 506–509.

(46) Meyer, B.; Padilla, J.; Vanderbilt, D. Theory of $PbTiO_3$, $BaTiO_3$, and $SrTiO_3$ Surfaces. *Faraday Discussions* **1999**, *114*, 395–405.

(47) Fong, D. D.; Stephenson, G. B.; Streiffer, S. K.; Eastman, J. A.; Auciello, O.; Fuoss, P. H.; Thompson, C. Ferroelectricity in Ultrathin Perovskite Films. *Science* **2004**, *304*, 1650–1653.

(48) Meyer, R.; Vailionis, A.; McIntyre, P. Direct Observation of Polarization vs. Thickness Relation in Ultra-Thin Ferroelectric Films. *arXiv preprint arXiv:0704.2441* **2007**,

(49) Giannozzi, P.; Baroni, S.; Bonini, N.; Calandra, M.; Car, R.; Cavazzoni, C.; Ceresoli, D.; Chiarotti, G. L.; Cococcioni, M.; Dabo, I. et al. QUANTUM ESPRESSO: a Modular and Open-Source Software Project for Quantum Simulations of Materials. *J. Phys.: Condens. Matter* **2009**, *21*, 395502.

(50) Fletcher, R. Practical Method of Optimization, Unconstrained Optimization, vol. 1. 1980.

(51) Perdew, J. P.; Burke, K.; Ernzerhof, M. Generalized Gradient Approximation Made Simple. *Phys. Rev. Lett.* **1996**, *77*, 3865.

(52) Perdew, J. P.; Ruzsinszky, A.; Csonka, G. I.; Vydrov, O. A.; Scuseria, G. E.; Constantin, L. A.; Zhou, X.; Burke, K. Restoring the Density-Gradient Expansion for Exchange in Solids and Surfaces. *Phys. Rev. Lett.* **2008**, *100*, 136406.

(53) Vanderbilt, D. Soft Self-Consistent Pseudopotentials in a Generalized Eigenvalue Formalism. *Phys. Rev. B* **1990**, *41*, 7892.

(54) Quantum ESPRESSO Pseudopotentials Library. http://www.quantum-espresso.org/pseudopotentials/, accessed April 8, 2017.

(55) Monkhorst, H. J.; Pack, J. D. Special Points for Brillouin-Zone Integrations. *Phys. Rev. B* **1976**, *13*, 5188.

(56) Bengtsson, L. Dipole Correction for Surface Supercell Calculations. *Phys. Rev. B* **1999**, *59*, 12301.

(57) Meyer, B.; Vanderbilt, D. Ab Initio Study of $BaTiO_3$ and $PbTiO_3$ Surfaces in External Electric Fields. *Phys. Rev. B* **2001**, *63*, 205426.

(58) Anisimov, V. I.; Zaanen, J.; Andersen, O. K. Band Theory and Mott Insulators: Hubbard U instead of Stoner *I. Phys. Rev. B* **1991**, *44*, 943–954.

(59) Anisimov, V. I.; Solovyev, I.; Korotin, M.; Czyżyk, M.; Sawatzky, G. Density-Functional Theory and NiO Photoemission Spectra. *Phys. Rev. B* **1993**, *48*, 16929.

(60) Liechtenstein, A.; Anisimov, V.; Zaanen, J. Density-Functional Theory and Strong Interactions: Orbital Ordering in Mott-Hubbard Insulators. *Phys. Rev. B* **1995**, *52*, R5467.

(61) Cococcioni, M.; De Gironcoli, S. Linear Response Approach to the Calculation of the Effective Interaction Parameters in the LDA+U Method. *Phys. Rev. B* **2005**, *71*, 035105.

(62) Himmetoglu, B.; Floris, A.; Gironcoli, S.; Cococcioni, M. Hubbard-Corrected DFT Energy Functionals: The LDA+U Description of Correlated Systems. *Int. J. Quantum. Chem.* **2014**, *114*, 14–49.

(63) Mattioli, G.; Alippi, P.; Filippone, F.; Caminiti, R.; Amore Bonapasta, A. Deep versus Shallow Behavior of Intrinsic Defects in Rutile and Anatase TiO_2 Polymorphs. *J. Phys. Chem. C* **2010**, *114*, 21694–21704.

(64) Agapito, L. A.; Curtarolo, S.; Nardelli, M. B. Reformulation of DFT+U as a Pseudohybrid Hubbard Density Functional for Accelerated Materials Discovery. *Phys. Rev. X* **2015**, *5*, 011006.

(65) Lichtenstein, A.; Anisimov, V.; Katsnelson, M. *Electronic Structure and Magnetism of Correlated Systems: Beyond LDA*; Springer, 2003; Vol. 54; p 101.

(66) Piskunov, S.; Heifets, E.; Eglitis, R.; Borstel, G. Bulk Properties and Electronic Structure of $SrTiO_3$, $BaTiO_3$, $PbTiO_3$ Perovskites: An Ab Initio HF/DFT Study. *Comput. Mat. Sci.* **2004**, *29*, 165–178.

(67) Brivio, F.; Butler, K. T.; Walsh, A.; Van Schilfgaarde, M. Relativistic Quasiparticle Self-Consistent Electronic Structure of Hybrid Halide Perovskite Photovoltaic Absorbers. *Phys. Rev. B* **2014**, *89*, 155204.

(68) Perdew, J. P.; Ernzerhof, M.; Burke, K. Rationale for Mixing Exact Exchange with Density Functional Approximations. *J. Chem. Phys.* **1996**, *105*, 9982–9985.

(69) Ernzerhof, M.; Perdew, J. P.; Burke, K. Coupling-Constant Dependence of Atomization Energies. *Int. J.Quantum Chem.* **1997**, *64*, 285–295.

(70) Ernzerhof, M.; Scuseria, G. E. Assessment of the Perdew–Burke–Ernzerhof Exchange-Correlation Functional. *J. Chem. Phys.* **1999**, *110*, 5029–5036.

(71) Adamo, C.; Barone, V. Toward Reliable Density Functional Methods without Adjustable Parameters: The PBE0 Model. *J. Chem. Phys.* **1999**, *110*, 6158–6170.

(72) SG15 Collection of Optimized Norm-Conserving Vanderbilt (ONCV) Pseudopotentials. http://fpmd.ucdavis.edu/qso/potentials/sg15_oncv/, accessed April 8, 2017.

(73) Hamann, D. Optimized Norm-Conserving Vanderbilt Pseudopotentials. *Phys. Rev. B* **2013**, *88*, 085117.

(74) Glazer, A.; Mabud, S. Powder Profile Refinement of Lead Zirconate Titanate at Several Temperatures. II. Pure $PbTiO_3$. *Acta Crystallogr., Sect. B: Structural Crystallography and Crystal Chemistry* **1978**, *34*, 1065–1070.

(75) DFT Optimised Crystal Structures of Inorganic and Hybrid Halide Perovskites. https://github.com/WMD-Bath/Hybrid-perovskites/ (accessed April 8, 2017).

(76) Brehm, J. A.; Takenaka, H.; Lee, C.-W.; Grinberg, I.; Bennett, J. W.; Schoenberg, M. R.; Rappe, A. M. Density Functional Theory Study of Hypothetical $PbTiO_3$-Based Oxysulfides. *Phys. Rev. B* **2014**, *89*, 195202.

(77) Yamada, Y.; Nakamura, T.; Endo, M.; Wakamiya, A.; Kanemitsu, Y. Near-Band-Edge Optical Responses of Solution-Processed Organic–Inorganic Hybrid Perovskite $CH_3NH_3PbI_3$ on Mesoporous TiO_2 Electrodes. *Appl. Phys. Express* **2014**, *7*, 032302.

(78) Kitazawa, N.; Watanabe, Y.; Nakamura, Y. Optical Properties of $CH_3NH_3PbX_3$ (X= Halogen) and Their Mixed-Halide Crystals. *J. Mat. Sci.* **2002**, *37*, 3585–3587.

(79) Butler, K. T.; Kumagai, Y.; Oba, F.; Walsh, A. Screening Procedure for Structurally and Electronically Matched Contact Layers for High-Performance Solar Cells: Hybrid Perovskites. *J. Mat. Chem. C* **2016**, *4*, 1149–1158.

(80) Liu, G.; Nan, C.-W. Thickness Dependence of Polarization in Ferroelectric Perovskite Thin Films. *J. Phys. D: Appl. Phys.* **2005**, *38*, 584.

(81) Sai, N.; Kolpak, A. M.; Rappe, A. M. Ferroelectricity in Ultrathin Perovskite Films. *Phys. Rev. B* **2005**, *72*, 020101.

(82) Baldereschi, A.; Baroni, S.; Resta, R. Band Offsets in Lattice-Matched Heterojunctions: a Model and First-Principles Calculations for GaAs/AlAs. *Phys. Rev. Lett.* **1988**, *61*, 734.

(83) Singh-Miller, N. E.; Marzari, N. Surface Energies, Work Functions, and Surface Relaxations of Low-Index Metallic Surfaces from First Principles. *Phys. Rev. B* **2009**, *80*, 235407.

(84) Eglitis, R.; Vanderbilt, D. Ab Initio Calculations of $BaTiO_3$ and $PbTiO_3$ (001) and (011) Surface Structures. *Phys. Rev. B* **2007**, *76*, 155439.